H$_2$O Maser Observations of Planetary Nebula K3-35

Blake Stauffer

A senior thesis submitted to the faculty of
Brigham Young University
in partial fulfillment of the requirements for the degree of

Bachelor of Science

Victor Migenes, Advisor

Department of Physics and Astronomy

Brigham Young University

April 2012

ABSTRACT

H$_2$O Maser Observations of Planetary Nebula K3-35

Blake Stauffer
Department of Physics and Astronomy
Bachelor of Science

Evolutionary processes of late type stars can be studied by using their maser emission as probes. Current models show that the environment inside a planetary nebula cannot support maser emission. The target, planetary nebula PN K3-35, has maser emission that is unexplained. The mechanics of radio interferometry and data reduction using the Astronomy Image Processing System are explained to show how the conclusions are obtained. Observation of the nebula does not reveal the mechanism for maser radiation, but results in a kinematic model of the maser regions in PN K3-35. Two 22 GHz water maser regions are present with a flux of 14 Jy above the continuum flux of 6 Jy.

ACKNOWLEDGMENTS

Contents

List of Figures

Chapter 1

Introduction

1.1 Astronomical Background

The aim of this thesis is the physics of maser emission in a planetary nebula environment. This has only been observed in one case: PN K3-35. By mapping the maser radiation and its subsequent motion in the planetary nebula, we gain a greater understanding of the science involved in old expanding stars, which often have explosive ends. Maser spots act as probes into stellar atmospheres. Currently, these are being used to determine mass loss rates into the interstellar medium. The ultimate goal is to use maser regions to predict novas or other cataclysmic events.

Planetary nebulae are the result of late stellar evolution in Aysmptotic Giant Branch (AGB) stars. When fusionable materials run out in the interior of the star, the atmosphere is no longer sustained by the pressure created by the reaction and collapses. The atmosphere rebounds off the degenerate core and out into space. This material is the planetary nebula. The degenerate core remains in its center as a white dwarf. The gases in the nebula are excited by constant radiation from the white dwarf. As the electrons in the cloud cascade down energy levels, photons are emitted. The low density of the cloud ensures that the majority of the photons escape. This
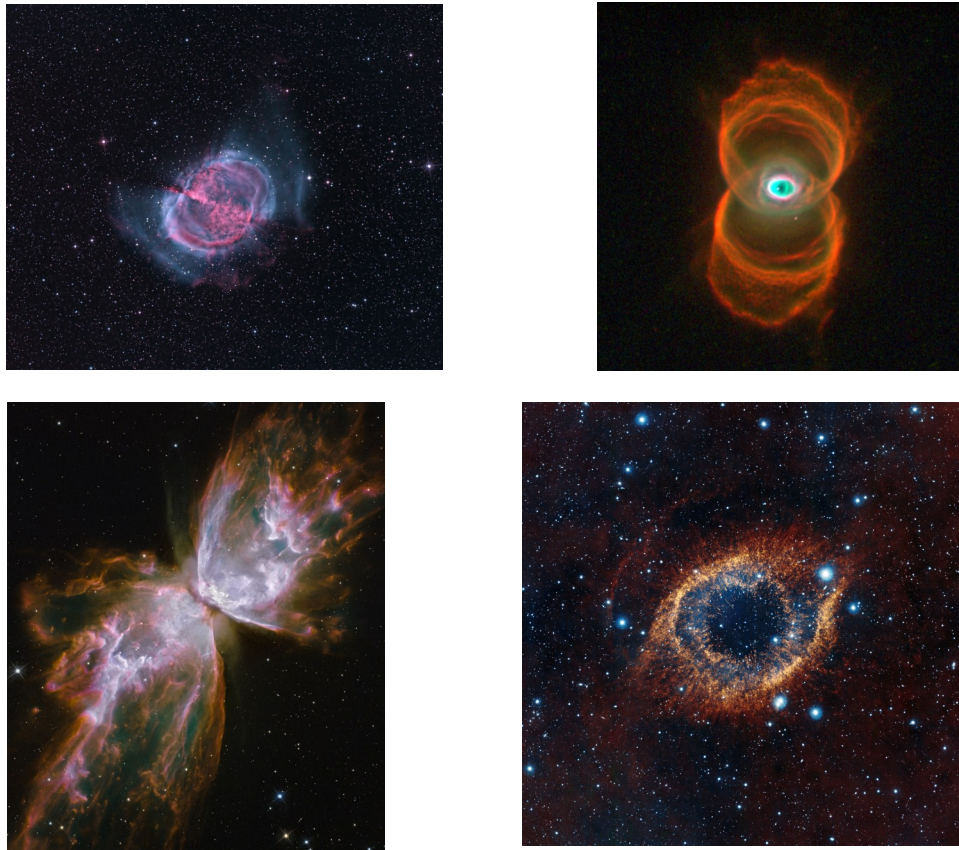
Figure 1.1 Images of planetary nebulae, courtesy of NASA.

radiation is mostly in the visible spectrum, but some are also in the ultraviolet. The low densities make collisional de-excitation extremely rare, resulting in the appearance of forbidden lines in its spectrum. The 500.68 nm and 495.89 nm lines from [O III] are frequently used to measure the cloud density (Carroll & Ostlie 2007). [O II] and [Ne III] are other forbidden lines visible in the the spectrum that are also useful in determining density. As evidenced by observing Doppler-shifted spectral lines, the planetary nebula moves away from the white dwarf at a speed anywhere from 10-30 km s^{-1}. Most observed planetary nebulae are 0.3 pc in diameter. This expansion into the interstellar medium causes the cloud to dissipate over a period of approximately 50 000 years, as the gases become too optically thin to remain excited. The expansion of the gas, combined with its decreasing temperature do not continue to support maser emission (Carroll & Ostlie 2007).

In relation to stellar atmospheres, maser radiation is only found in stellar envelopes of highly evolved stars. The end processes of theses stars involves significant mass loss into the interstellar medium. Late type AGB stars undergo this process as they gradually transform into planetary nebulae. However, current astrophysical models are insufficient to explain the presence of maser radiation in the evolved form of AGB stars.

1.2   Previous Work on K3-35

The target, PN K3-35, has been studied extensively in the past (Tafoya et al. 2007) (Gomez et al. 2009) (Tafoya et al. 2011). It is identified as a proto planetary nebula that experiences mass loss in a torus around the equatorial region (Uscanga et al. 2008). There are also outflows at each of the poles (Uscanga et al. 2008). At that time the peak flux in maser radiation was about 1572 mJy (Uscanga et al. 2008). The torus has a rotational velocity of 3.1 km s^{-1} and expanding at a rate of 1.4 km s^{-1} (Uscanga et al. 2008). Observation of the 22 GHz line reveals a systemic velocity of 20.88 - 23.00 km s^{-1} in relation to the Local Standard of Rest (LSR) (Tafoya et al. 2011). Its distance is estimated to be 5 kpc (Tafoya et al. 2011).

Hydroxyl (OH) masers were identified in 2009, at 1665 and 1720 MHz (Gomez et al. 2009). They are distributed around the core of the nebula, while the previously observed water masers are present in the outer envelope. Peak observed flux was 1496.6 mJy (Gomez et al. 2009).

Three H_2O maser features detected in 2011 (Tafoya et al. 2011). More detailed observation in infrared indicates that K3-35 has a total ionized mass of about 9x10^{-3} M$\odot$ (Tafoya et al. 2007). This total ionized material is inconsistent with known conditions for maser radiation.

1.3   Maser Physics

The maser characteristics of astronomical hydroxyl maser emission were first observed in 1965. Water maser emission was later observed by Cheung in 1969. Water masers were discovered to be more compact in size and produce larger intensities than the hydroxyl masers (Carroll & Ostlie 2007). More complex molecules with maser properties were later discovered such as CH_3OH and SiO (Carroll & Ostlie 2007). Higher intensity radiation was then observed in the cores of galactic nuclei and was classified as megamasers. Maser emission is from observed in star forming regions, HII regions, supernova remnants, and stellar envelopes of stars.

Maser stands for Microwave Amplification by Stimulated Emission of Radiation. The term has been colloquially shortened to "maser" just as the term laser. Microwaves are classified in the radio regime of the electromagnetic spectrum. As such, masers are not limited microwaves, but also included stimulated emission of radio waves. A maser functions similar to a laser in that it is caused by stimulated emission when a population inversion occurs in molecular gas. The energy transitions that occur involve changing rotational states within a molecule. These lower energy transitions produce radio waves as opposed to visible light. The lower energy interactions are observed frequently in nature, whereas laser emission has never been observed naturally by account of its higher energy requirements. (Cohen 1989)

Maser radiation is not thermal in nature. This is significant because all other non radio sources of astronomical radiation are caused by continuum radiation from a blackbody like object. Masers are best described using the model of the three level atom. Incoming infrared photons serve as a heating mechanism, pushing electrons in the water molecule into a higher rotational state. They then decay into a slightly lower energy state. The second de-excitation is a result of spontaneous emission, and the radio photon is emitted. Its interaction with a second molecule in the second excited state causes stimulated emission, and a second radio photon is emitted with the same phase and wavelength as the first. As this process repeats among the many molecules in a gas, there is a
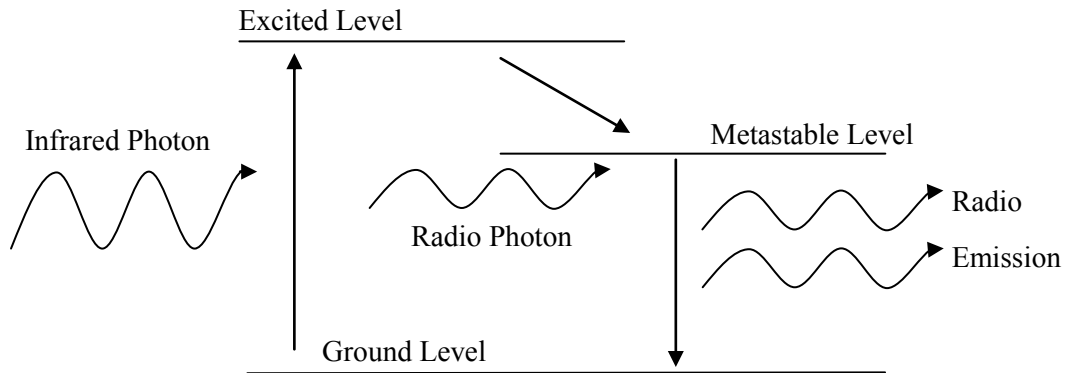
Figure 1.2 Masing species follow the model of a three level rotational energy diagram. Infrared photons pump the molecule into the top excited state. They then fall to the metastable level spontaneously. The third transition is a result of stimulated emission.

significant amplification of the radio signal. This signal has the largest intensity of radiation ever observed in astronomy. (Dopita & Sutherland 2003) See Fig. 1.2 for details.

The conditions for maser radiation are very specific, which allows us to examine the conditions of where they occur. This is very important to understanding where and why they occur in astronomy. The gaseous regions must first be very dense, about 10^6-10^{11} molecules cm^{-3}, depending on the masing species (Dopita & Sutherland 2003). Temperature is also an important condition, depending on how it is defined. Excitation temperature, defined by the velocity distribution of the molecules, must be approximately 200 K (Dopita & Sutherland 2003). Brightness temperatures must be in the 10^9-10^{12} K range (Dopita & Sutherland 2003). The radio radiation produced is very narrow in bandwidth and is highly collimated. The radiation is also circularly polarized because of the phase shifts from the delays in stimulated emission. If the maser region is close to the thermal source of the infrared pumping radiation, it often becomes saturated, and the stimulated radio radiation continues linearly with the pumping mechanism (Dopita & Sutherland 2003).

Maser radiation occurs in multiple wavelengths, which allows us to identify the species of molecule that is involved. The most commonly observed frequencies are 1665, 1667, 1612, and 1720 MHz caused by hydroxyl. Hydrogen cyanide (89 GHz) and methanol (12 GHz) have also

been observed in star forming regions.

1.4   Overview

The data for this project comes from the Very Large Baseline Array (VLBA), a series of radio telescopes spread around the United States. The raw data was accessible from the National Radio Astronomy Observatory (NRAO) archives. It was taken in September of 2003. The Astronomical Image Processing System (AIPS) is the primary tool for reducing the data. The specific procedure for reducing the data is illustrated in Fig. 1.3 and described in Sec. 2.2.

```
┌─────────────────────┐
│ FITLD: Load Data    │
└─────────────────────┘
           │
           ▼
┌─────────────────────────────────────┐
│ ANTAB: Amplitude and phase calibration │
└─────────────────────────────────────┘
           │
           ▼
┌──────────────────────────────────────┐
│ CLCAL: Amplitude and phase interpolation │
└──────────────────────────────────────┘
           │
           ▼
┌──────────────────────────┐
│ FRING: Phase referencing │
└──────────────────────────┘
           │
           ▼
┌────────────────────────┐
│ IMAGR: Generates image │
└────────────────────────┘
           │
           ▼
┌─────────────────────────┐
│ JMFIT: Analysis of image │
└─────────────────────────┘
```
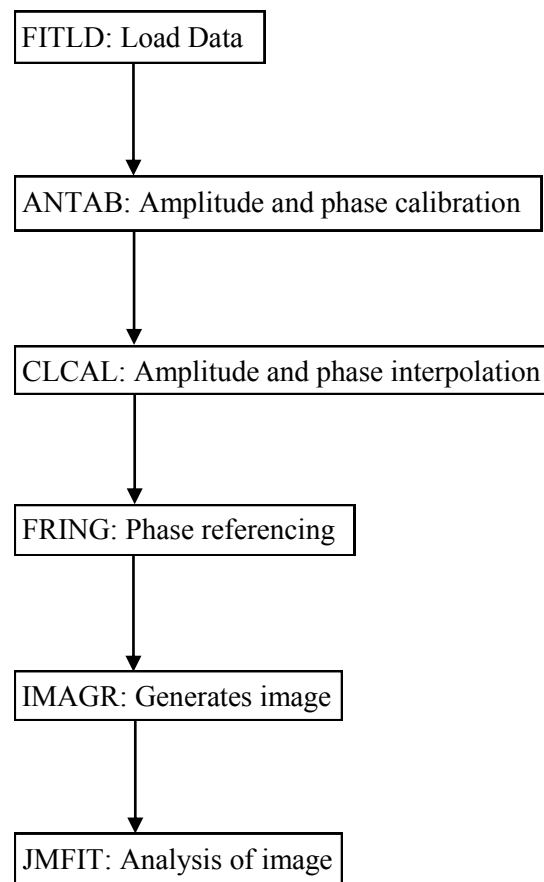
Figure 1.3 Reduction process of AIPS. Explained in detail in Sec. 2.2.

Chapter 2

Observations And Data Reduction

2.1   Radio Telescopes

Observation of PN K3-35 took place over eight hours of observation on September 13, 2003 using the Very Large Baseline Array (VLBA). The VLBA is a network of ten radio antennas spread around the United States to create a large effective diameter for the telescope. Each pair of antennas creates an interferometer, also known as a baseline. The longest baseline is between the St. Croix and Mauna Kea antennas at 8611 km. This is also the maximum effective diameter for the radio telescope. The total number of telescopes allows for 45 baselines. See Fig. 2.1. The advantage of many baselines is explained later in the section.

Radio astronomy provides an advantage over optical astronomy: the wavelengths are long enough that the gain from the antennas can be time-referenced to sufficient accuracy that phase delays in the light wave can be measured. The large wavelengths allows radio interferometry, unlike optical wavelengths, which are too short for interferometry. Instead of using one large telescope to gain a large signal or high angular resolution, multiple telescopes are used to collect data on a single source. Every two antennas can be used as a baseline. A baseline interferometer

Figure 2.1 Map of the VLBA, courtesy of NRAO.

is similar to the double-slit interferometer. In this setup, a plane wave from a distant source is incoming on a double slit, or in this case, the two antennas of a baseline. The signal obtained from correlating (or superposing) the individual signals from each antenna displays a fringe pattern. At a later time, the fringe pattern can be deconvolved from the point source response of all the baselines in the telescope. This response is known as the beam pattern of the telescope. Fig. 2.2 gives an example of the resultant pattern when all of the baseline beams in the VLBA are vector averaged.

Although the baseline of the VLBA is significant, it has reduced light-gathering power compared to arrays that contain more antennas. The VLBA's limited number of antennas limits the resolution of its beam pattern, making the image it creates difficult to resolve. Fortunately, the earth's rotation partially mitigates this problem. As the earth rotates, the relative positions of the antennas change with respect to the source. This has the effect of altering the length of the baselines. It also introduces phase delay (See Fig. 2.3). Fortunately, the positions of each antenna is precisely known and calibrated using an atomic clock so that the delay can be accounted.
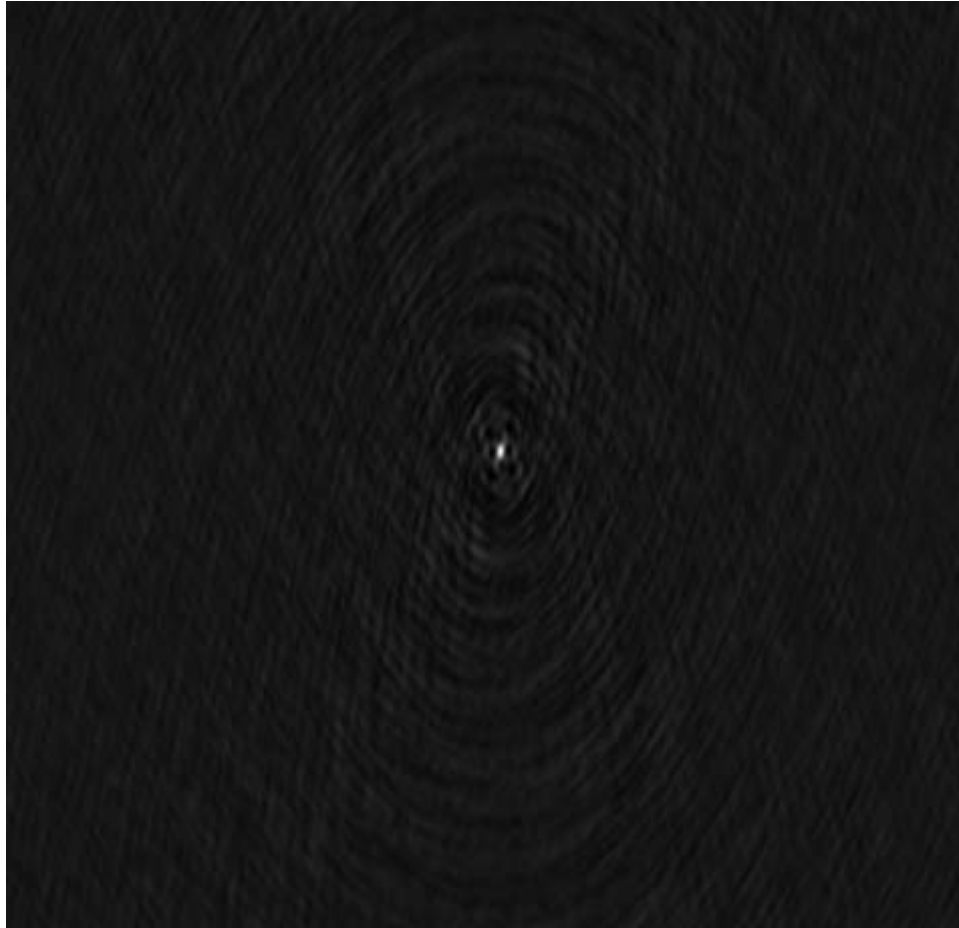
Figure 2.2 Beam pattern for the VLBA. It is constructed by convolving the beams of each of the antennas in the array over the course of observation. This beam pattern is used to remove the fringe pattern in the VLBA's image.
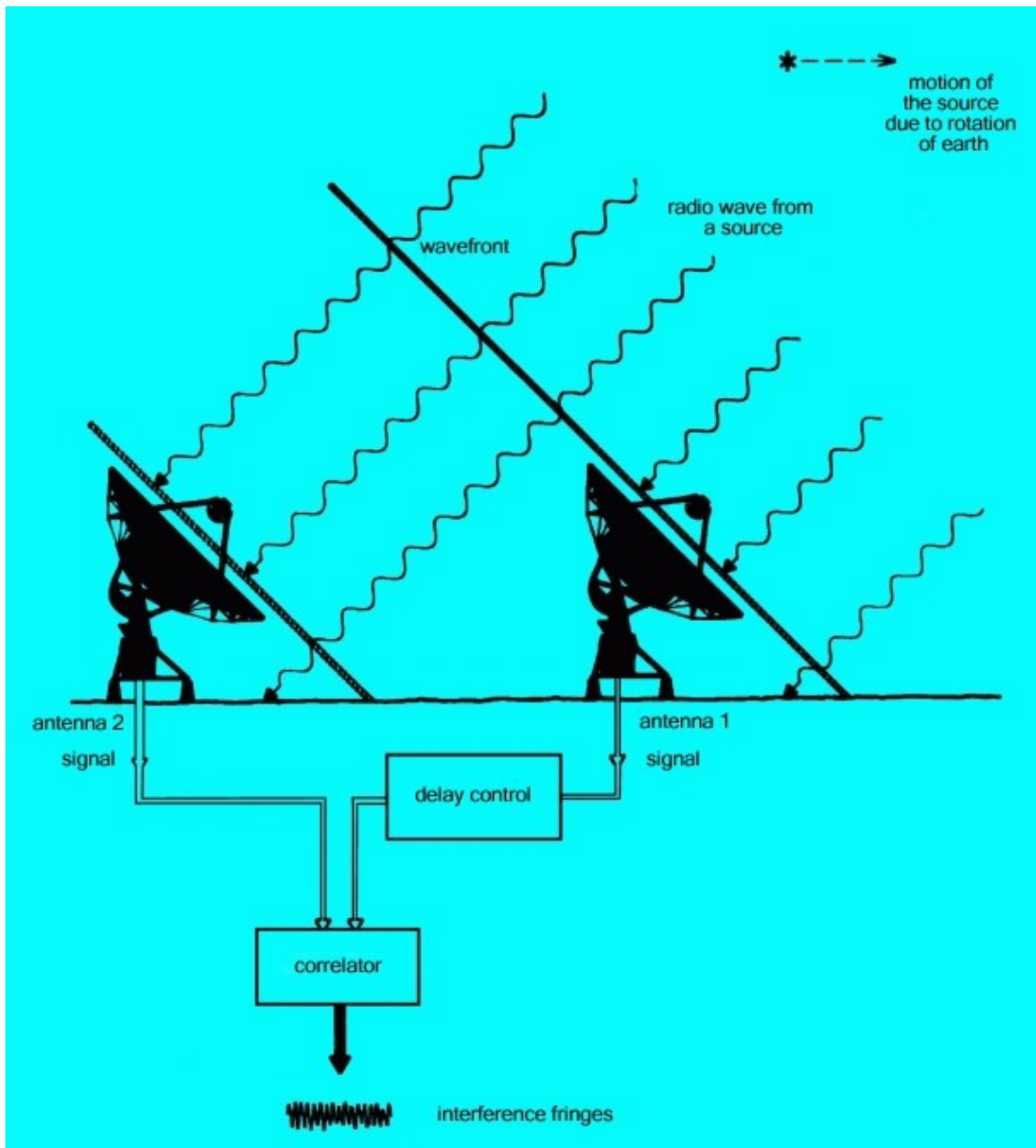
Figure 2.3 Light from a distant star approach the radio antennas as plane waves. The correlator combines the signal from each antenna and corrects for the delay in the receipt of each wave. This corrects for the phase delay that occurs as a result of the earth's motion and the placement of each antenna in the array. Source: http://www.scienzagiovane.unibo.it/
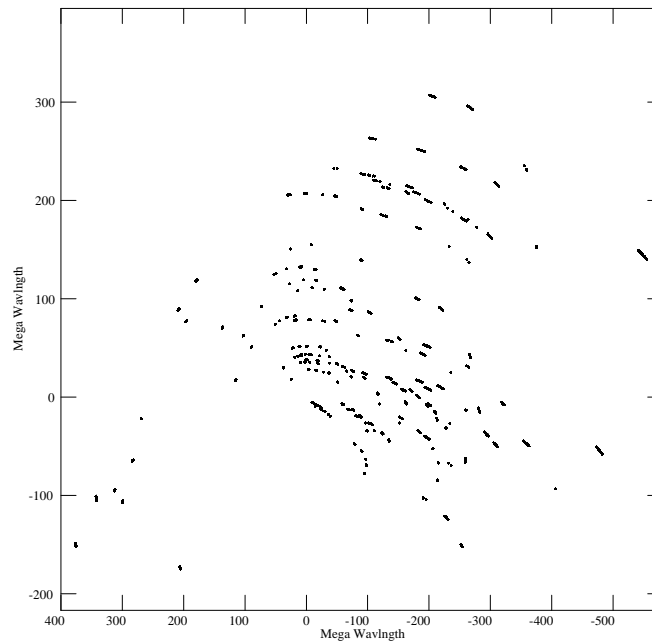
Figure 2.4 This represents the UV plane, or plane wave from the observed source. Each point is known as a visibility. The distance between two points corresponds to a baseline. More visibilities grants greater detail in determining the beam pattern. For simplicity, only one out of 1111 visibilities are plotted.

During observation, each integration of an observation from a baseline creates a single point of data called a visibility. Throughout the observation sequence, visibilities are collected and contain information such as effective baseline length and signal strength. When the sequence is complete, the visibilities are displayed on a graph called the UV plane. The UV plane models the plane wave incoming from the source. As each visibility is taken, it generates a point in the UV plane. With a larger baseline, the visibilities are more spread out, and greater angular resolution is obtained. As the earth rotates, the antennas sweep out additional baseline lengths. Filling the UV is advantageous as it allows for a more detailed beam pattern. Few visibilities limits knowledge of the beam pattern, which makes the image formed the array difficult to resolve. See Fig. 2.4 for more details.

An antenna in an array is simply a point detector. Only radio flux (or signal) is measured by each antenna. The convolution of each antenna's signal to the visibilities in the UV plane generate the image of the source. Once the image is obtained, it must be deconvolved with the previously determined beam pattern of the array. This is done using phase reference data, obtained by either observing a standard continuum source, or by using reduction software to model potential source types to deconvolved the image one step at a time. See Fig. 2.2.

2.2   AIPS Reduction

2.2.1   Loading Data

The standard tool for reducing radio data for the National Radio Astronomy Observatory (NRAO) is the Astronomical Image Processing System (AIPS). AIPS is available to use on Linux operating systems and was provided by Brigham Young University as a courtesy. The data from PN K3-35 comes from the NRAO archive. It is now part of the public domain.

Raw data is stored in image files called fits (with the extension .fits), as is standard for the NRAO. .fits files, however, are limited in size and must be uploaded in several stages. Data on PN K3-35 was included in eight .fits files. The data was uploaded into AIPS with the fitload (FITLD) task. Once it was uploaded, it was concatenated using a task that sorts the data with respect to time of observation (UVSRT). UVSRT references the time table of the data set to order the observations.

2.2.2   Corrections to the Data

Each antenna in the area is different and is subjected to differing atmospheric and ionospheric conditions. To account for the differences, each antenna records its temperature, gain, and phase characteristics, which are appended to the .fits files in calibration tables. An important calibration table is the flag (FG) table. This table contains information about various errors that occur during

observation, such as malfunctioning mounts and errors in phase data. This table is used to eliminate bad visibilities from the data set without erasing the visibilities themselves. Once the reduction is complete, all the calibration tables are applied to the data set to create the solution.

Another table includes the system temperature of each antenna. The response of an individual antenna to the incoming signal is the gain. Temperature predictably affects the gain of each antenna depending on the wavelength that is being observed. The array was set to observed 22 GHz line emission, so appropriate gain correction was applied.

The SN table from the data set contains the positions of the antennas and thus their phase delay information. It also contains data on the gain for each antenna. The task ANTAB applies the amplitude correction for each antenna. Fig. 2.5 gives examples of the amplitude data for four of the baselines in the array. ANTAB also corrects the phase delay in each of the baselines. Fig. 2.6 gives examples of the phase correction data for four of the baselines.

The correctional data, however, is not immediately applied to the data set. Instead, it is stored in a calibration table (CL). The amplitude and phase information tables are limited. Not every visibility has a corresponding phase delay or amplitude correction. This leaves large gaps in the calibration for the visibilities that are not labeled. Applying the calibration correction task (CLCAL) to the unlabeled visibilities uses linear interpolation to approximate the amplitude and phase information across the gaps.

The baseline length data contained in each visibility can be plotted. The result is Fig. 2.4. The gain of each visibility can also be compared with baseline length (Fig. 2.7). Any outlying visibilities in the data can be added to FG table so that it can be ignored in the final solution. In this data set, all visibilities with a signal over 40 Jy were added to the FG table.
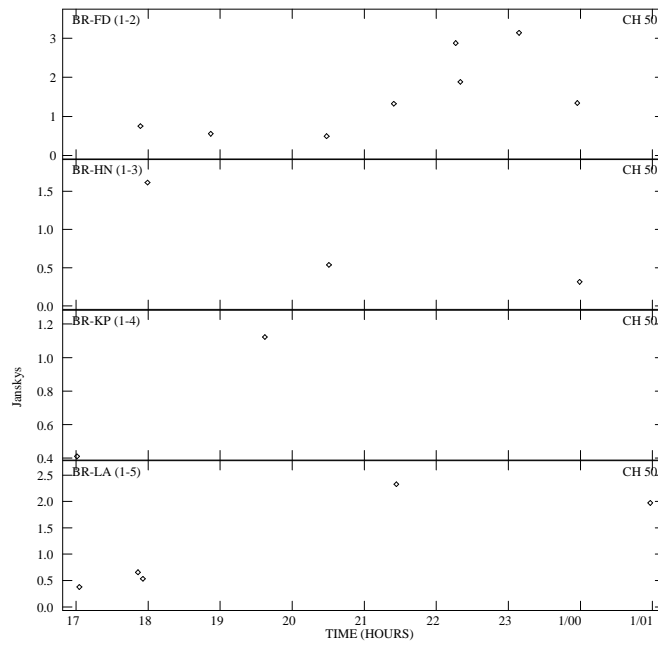
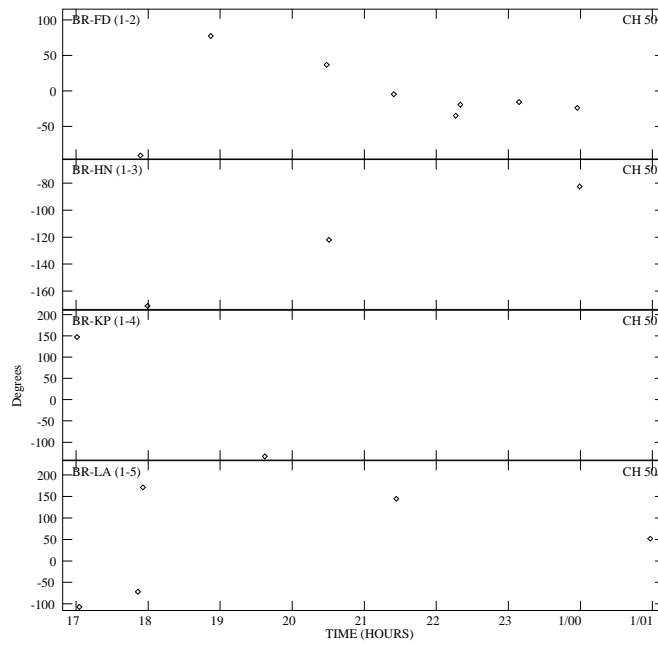**Figure 2.5** Amplitude correction for four sample baselines.

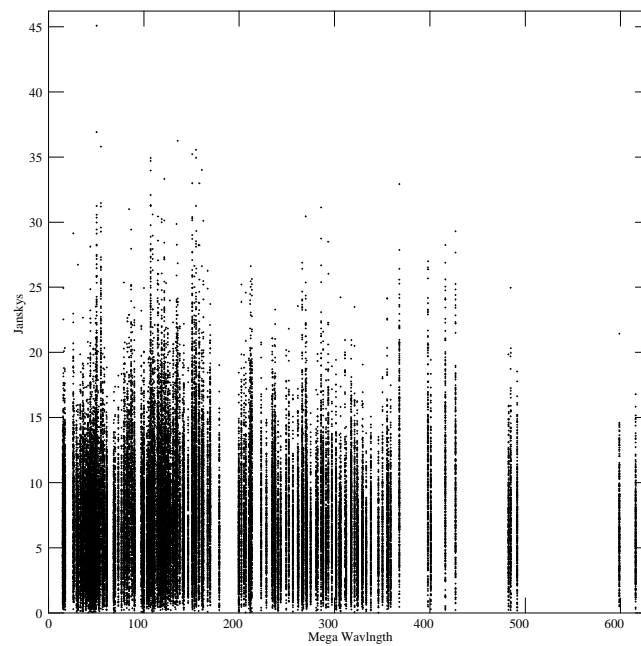**Figure 2.6** Amplitude correction for four sample baselines.

Figure 2.7 The gain for each of the visibilities. The U and V axis from Fig. 2.4 have been combined into the x-axis, which represents baseline length. The y-axis represents the gain for each visibility. For simplicity, only one out of 1111 visibilities are plotted.

2.2.3   Creating a Solution

Most radio arrays have multiple frequency channels (IF). The VLBA has two, so that two different wavelengths can be observed at the same time. The observation was only conducted on the 22 GHz emission line, so only one IF was required. However, polarization data was initially included in the separate IF channel. This was a mistake. We had to return to the FITLD task, reload the data into AIPS, and resort the data using the indexing and sorting tasks to append the data into the correct tables. Otherwise, the polarization of the radio wave would have interfered with the calibrated data set.

Each antenna in the array contains 256 channels. These channels sweep through electromagnetic spectrum in the 22 GHz range in small intervals to create a spectrum of the target. The spectrum difference is due to doppler shift based on the velocity of the target. Thus relative velocity is determined from the spectra of K3-35. This slices the target into discrete velocity intervals which are used to create a three dimensional greyscale image of the target. See Fig 2.8. The velocity was calibrated by using the same systemic velocity that was previously measured (Tafoya et al. 2011). The peak wavelength is centered on 21 km s^{-1}.

Amplitude calibration data is obtained by observing a standard continuum source of radio radiation (The standard used for this observation was J1925+2106). The standard has a well known constant flux in all channels. The data obtained from K3-35 has flux determined from the antenna gain, but does not account for interstellar or atmospheric absorbtion. By measuring the flux from the standard star just prior to observing the target, a scale factor for the losses is obtained. The scale factor is then applied to flux from PN K3-35 to obtain the true flux from the object.

Standard stars can also be used for finding good positions and improve sensitivity. This helps reduce the side lobes and noise level before considering self-calibration. Unfortunately, no phase referenced standard was provided with the data, necessitating the self-calibration described in Sec. 2.2.4.
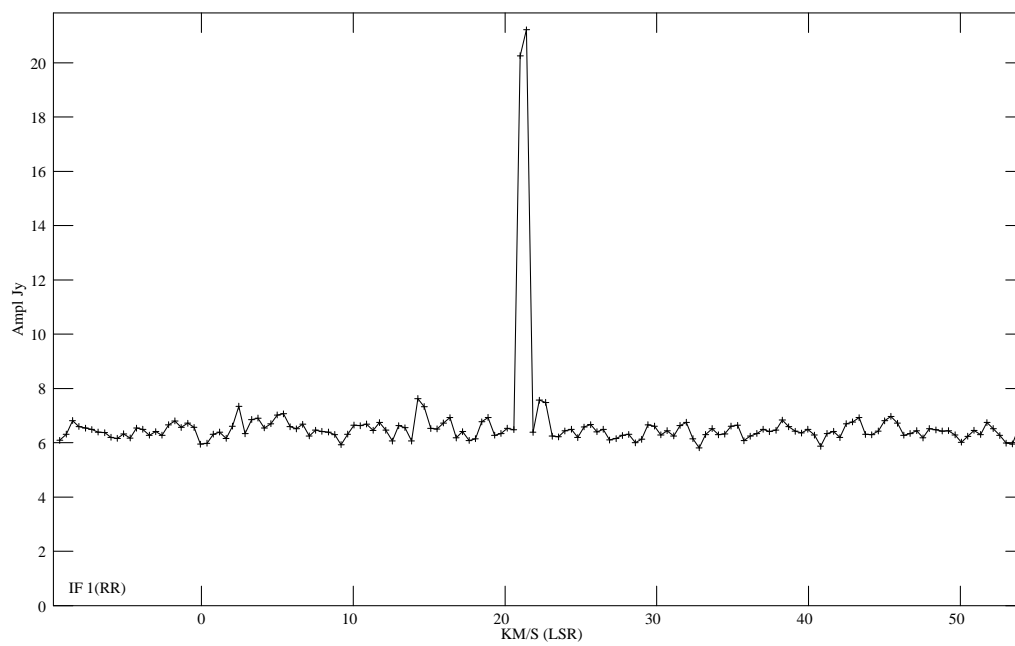
Figure 2.8 The spectra of PN K3-35. The spike in the center is the peak amplitude of the maser emission. It corresponds to a systemic velocity of 21 km s^{-1} with respect to the local standard of rest.

AIPS includes the fringe calibration task (FRING). This task attempts to improve the phase info by finely defining the fringe rate and delay in the generated image. The absence of phase referenced data hampers this task. This calibration does not better the reduced image of PN K3-35, so I have rejected the FRING calibration.

Once these calibration steps are complete, the calibration tables need to be applied to the data set. The task labeled CVEL splits the calibration table to the existing data and generates a new file for reduced data. This can be treated as a separate object from the original data. Thus the original data is preserved in case more correction is necessary.

2.2.4   Self-Calibration

AIPS imaging task (IMAGR) deconvolves the UV visibility data with the beam pattern (Fig. 2.2). This is done for each selected channel. Fig. 2.9 provides an example of an image from the peak channel. Notice how there are lobes surrounding the central maser spot. This is still a dirty image because it has yet to be cleaned. Then self-calibration attempts to remove the lobes.

IMAGR starts by assuming a point source for the object and generates a gaussian response to the modeled point source. The program then subtracts the same amount of flux from the lobes present in the image and adds it to the peak maser spot, where the point source is suspected to be. The program then repeats those steps in an iterative process attempting to account for all the flux outside of a point source. Once that is complete, a model for a double point source, or more extended object, can be applied to the image and then deconvolved in a similar process. This can be done to the modeler's satisfaction. Each iteration creates a solution. However, it is possible for the program to fail to generate a solution. The cleaning method I used iterated 200 times, with 2876 good solution and only 10 failed solutions. Each channel can be self-calibrated in the same way. It is only necessary to attempt the self calibration in the few channels surrounding the peak channel in the spectrum (Fig. 2.8).
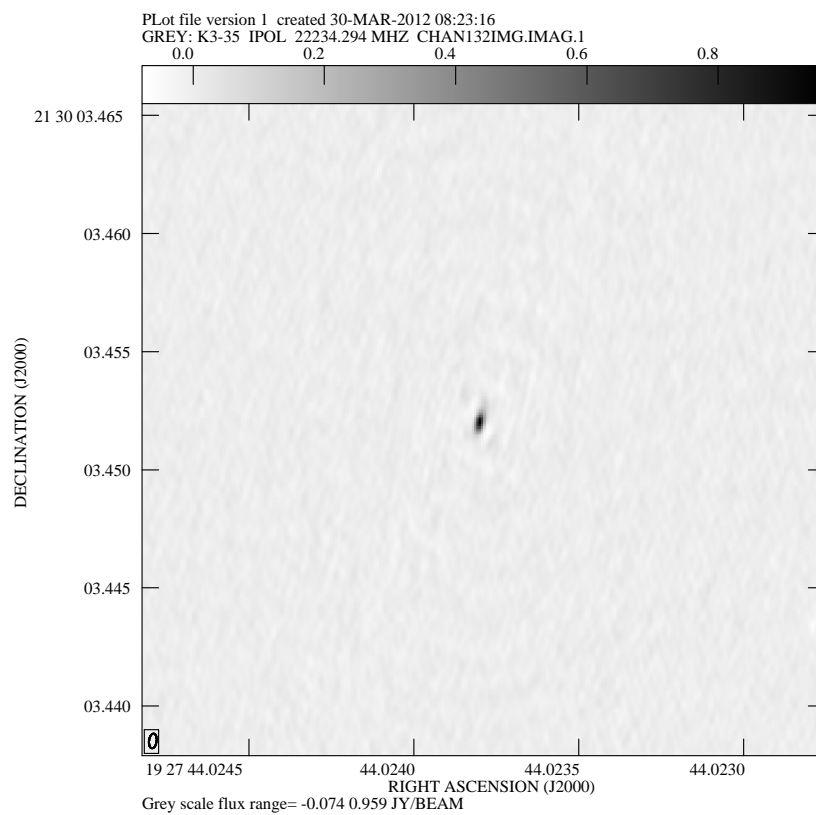
PLot file version 1 created 30-MAR-2012 08:23:16
GREY: K3-35 IPOL 22234.294 MHZ CHAN132IMG.IMAG.1

Grey scale flux range= -0.074 0.959 JY/BEAM

Figure 2.9 Image of the source for the peak flux channel.

V_{LSR}	Peak Intensity (Jy)	V_{LSR}	Peak Intensity (Jy)
26.5	0.30409	21.8	0.88548
26.1	0.07716	21.8	0.64438
25.6	0.34086	21.8	0.1533
25.2	0.11306	21.8	0.22323
24.8	0.41745	21.8	0.1186
24.4	0.13763	21.8	0.49912
23.9	0.55865	21.4	17.313
23.5	0.24308	21	16.97
23.1	0.8778	20.6	0.16723
23.1	0.26977	20.2	1.6723
22.7	3.8479	19.7	0.11395
22.3	1.452	19.3	0.95141
22.3	3.4141	18.5	0.64438
22.3	0.19197		

Table 2.1 Peak intensity for each maser region for each channel, converting channel into velocity with respect to the local standard of rest.

Now that a clean image is available, I can extract useful data from it. The task JMFIT reads data on selected regions of each image frame. I read peak intensity data from each frame. The results are in Table 2.1. JMFIT also provides location data and errors for each of the maser spots (included in Tab. 3.1).

Chapter 3

Discussion

3.1 Analysis

JMFIT analysis on the image map (See Sec. 2.2 and Fig. 2.9) results in the following table of values for the relative positions of the maser regions in each of the channels 3.1. This table is closely related to Fig. 2.8 where each channel near the peak has been examined. Each channel number is listed along with its corresponding V_{LSR} (Velocity with respect the the Local Standard of Rest). Each maser region in each image has an offset in degrees in the Right Ascension (RA) and Declination (DEC) relative to its center. The error in degrees in RA and DEC for each maser region is also calculated by JMFIT. The large effective diameter of the radio telescope allows for high precision in calculating these positions.

Since distances are difficult to determine in astronomy, the actual separation of the maser regions are unknown. The only thing that can be measured are the angular separation in the sky. This is done using an angular coordinate system that references celestial equator and the vernal equinox. Right ascension (RA) is the angular displacement of an object east of the vernal equinox, while declination (DEC) is the angular displacement from the celestial equator. The uncertainties

in each of the of the maser positions are included. The errors in RA and DEC can be examined while the error in velocity space is insignificant. If the separation of two maser regions is less than the calculated error, they can be safely assumed to be part of the same maser region.

Now we begin to model the maser regions in three dimensional space. Fig. 2.9 shows the maser regions along the line of sight. Fig. 3.1 shows the maser regions in RA and velocity space. The separation between the upper and lower sets of points are larger than their associated errors, indicating that there are at least two resolved regions in RA. The two center points are within the RA error parameters and are thus unresolved. This means that although we can see maser regions in this area, they cannot be identified as independent from the other two maser regions.

Fig. 3.2 shows the maser regions in DEC and velocity space. The majority of the data points are correlated with two maser regions. This is consistent with the two regions identified in the RA vs. velocity dispersion.

Although velocity is impossible to correlate to an angular displacement, the high linear correlation of the maser regions in velocity space is strong evidence that there are only two resolved maser regions.

Dispersion in velocity space is narrow. Sec. 2.2 describes the origin of the systemic velocity of 21 km s^{-1}. All maser regions are within 5 km s^{-1} of the systemic velocity. PN K3-35 therefore has low velocity dispersion.

The spectra of PN K3-35 (Fig. 2.8) shows a maser emission in all channels at about 6-7 Jy. This is not maser emission, but is background continuum radio radiation from PN K3-35. This comes from thermal rotational transitions within the planetary nebula. Thermal radio radiation is very low and is absorbed by the interstellar medium rather than amplified like maser emission. Continuum radiation can also be from galactic background from external sources. The continuum radiation is very low compared to the brief spike in emission caused by the maser regions. The continuum measurement of the radiation introduces error into calculating the flux in the maser

Channel	V_{LSR}	Relative RA	error RA	Relative DEC	error DEC
1	26.5	0.02380022	2.44E-07	0.4520074	6.89E-06
2	26.1	0.02279306	1.00E-07	0.443322	3.12E-06
3	25.6	0.02380001	2.18E-08	0.4520109	6.56E-06
4	25.2	0.02279287	7.24E-07	0.4433198	1.97E-05
5	24.8	0.02380012	1.17E-07	0.4519984	4.97E-06
6	24.4	0.02279316	6.03E-07	0.4433404	1.73E-06
7	23.9	0.02379954	1.51E-07	0.4520213	4.33E-06
8	23.5	0.02279368	3.70E-07	0.4433072	1.03E-05
9	23.1	0.0238007	1.04E-07	0.4520213	3.21E-06
9	23.1	0.02278758	4.05E-08	0.4432651	1.34E-05
10	22.7	0.02279211	6.70E-08	0.4133215	1.76E-06
11	22.3	0.02279211	6.70E-08	0.4520118	4.28E-06
11	22.3	0.02279351	6.79E-08	0.443323	1.93E-06
11	22.3	0.02319092	1.26E-06	0.4469422	1.06E-05
12	21.8	0.02381777	1.40E-07	0.4509515	4.13E-06
12	21.8	0.0237987	1.32E-07	0.4520228	3.84E-06
12	21.8	0.02392918	8.38E-07	0.4409791	2.02E-05
12	21.8	0.02319171	5.39E-07	0.4468905	1.70E-05
12	21.8	0.02279467	1.07E-06	0.4433699	2.96E-05
12	21.8	0.02380015	2.67E-07	0.4519775	1.62E-06
13	21.4	0.02379977	5.40E-08	0.4520083	1.62E-06
14	21	0.02379971	5.88E-07	0.452007	1.81E-06
15	20.6	0.02279361	5.82E-07	0.4433408	1.81E-05
16	20.2	0.02379976	7.30E-08	0.452037	2.48E-06
17	19.7	0.02279298	8.00E-07	0.4433257	2.90E-05
18	19.3	0.02380023	9.60E-08	0.4520266	2.96E-06
20	18.5	0.0237987	1.32E-07	0.4520228	3.84E-06

Table 3.1 Peak intensity regions and their relative angular separation in right ascension and declination.
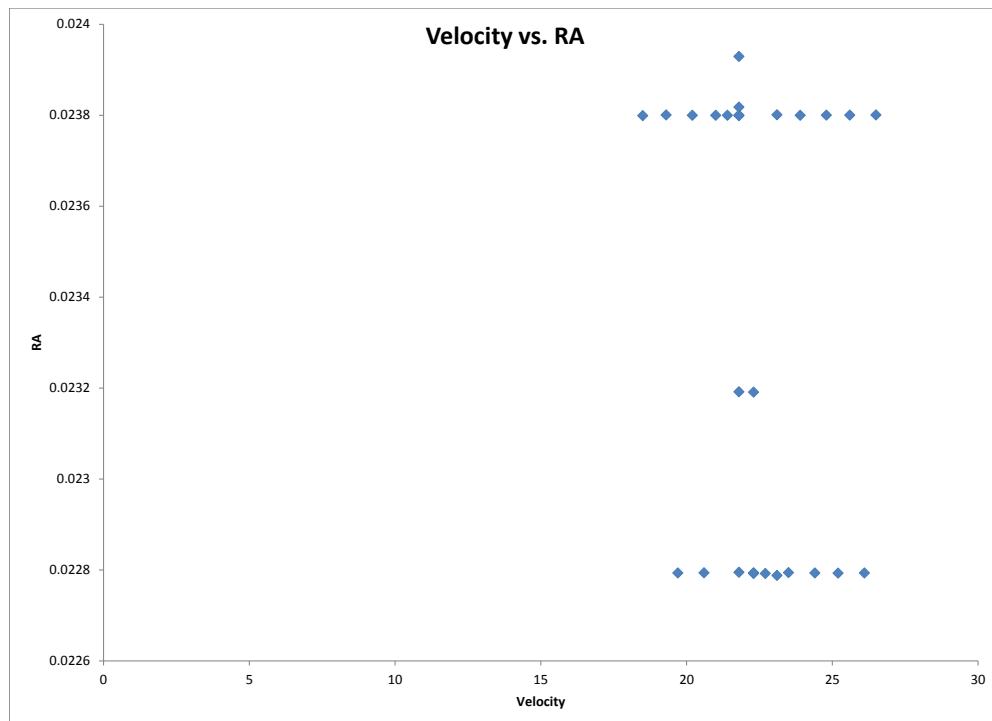
Figure 3.1 This shows the maser distribution in right ascension and velocity space. The line of sight is to the right on the graph. This is the view of the maser regions from the side.
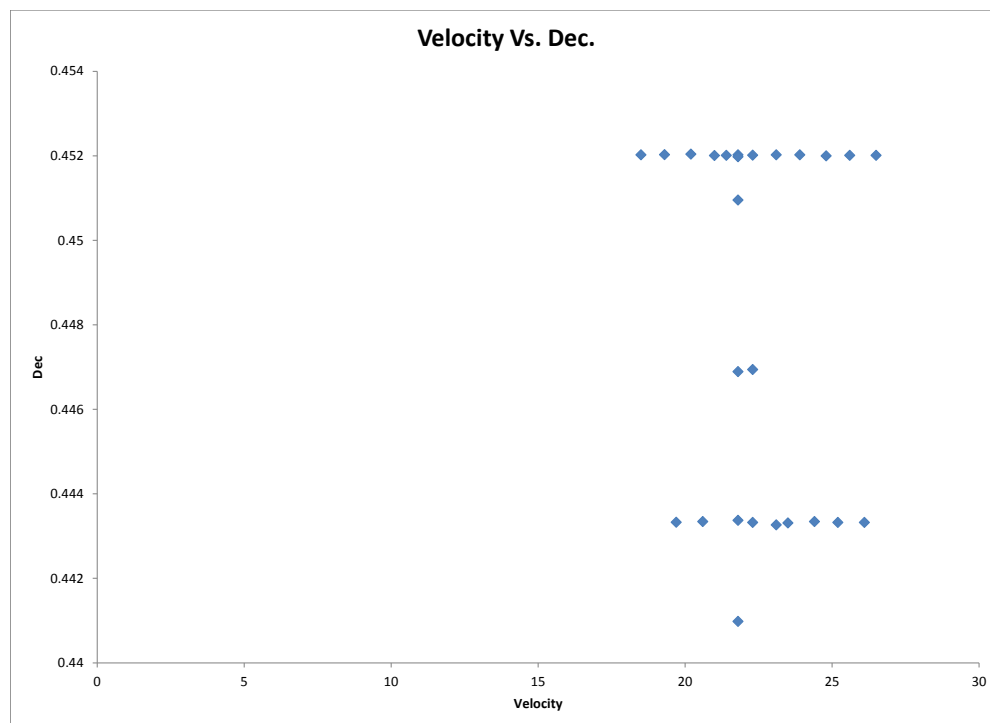
Figure 3.2 This shows the maser distribution in declination and velocity space. The upwards direction is in the line of sight. It is essentially a top down view of the maser region.

regions. The distribution is flat, which fortunately minimizes the error. Running JMFIT in the non masing regions of Fig. 2.9 reveals that the mean value of the radiation in those areas is uniform and constant.

Chapter 4

Conclusions

4.1 Results

Only two maser regions in PN K3-35 have been resolved using the VLBA data. Later observations from Uscanga (Uscanga et al. 2008) and Tafoya (Tafoya et al. 2007) using multiple single dish telescopes show more masing regions and at a lower intensity. It is likely that there are indeed more maser regions than the two observed here. The limiting factor is the sensitivity of the VLBA, which is limited to ten antennas. Further observations were conducted using the VLA, which has greater sensitivity while sacrificing resolution (See Sec. 2.1). Also, the beam from the VLBA is very small and has washed out the weaker and non-compact maser emission in the medium.

Decreases in the intensity of the radiation from the target were observed previously (Uscanga et al. 2008) (Tafoya et al. 2007). Their measurements are in the milliJansky range. This is consistent with stellar evolution models that maser regions disappear when a late type star transitions into a planetary nebula. However, the mere presence of maser emission is evidence that PN K3-35 is not a planetary nebula. Instead it suggests that PN K3-35 is still partly a late type star, even though optical and infrared data identify it as a planetary nebula. The evolution of the region is unknown.

The two spots that are resolved are insufficient to model mass flow from the region. All that we can conclude is that the masers indicate the presence of water in the stellar atmosphere. While it is possible for maser radiation exist within the region, the required conditions are not directly observed. However, the mere presence of maser infers the existence of those conditions in the region.

4.2 Directions for Further Work

Further study of PN K3-35 is needed to model the expansion of the maser regions in the interstellar medium. While it is reasonable to assume that the maser regions will weaken as the gas expands, the radiation is at a high enough intensity to expect it to be observable for many more years. However, as the physics of the region are still not well understood, the timescale for the decrease in maser radiation to below a detectable level is unknown. Our best estimate is that the radiation will only last a couple more decades. Tracking the proper motion of the maser regions will allow for the determination of size and rate of expansion once better estimates of distance have been obtained. Observations of the decrease in maser intensity can also help build models for what is causing the maser radiation and the expansion of the shell.

PN K3-35 is also a prototype for identifying other planetary nebulae with maser emission. While PN K3-35 is the only identified object of its kind, we speculate that it is unlikely to be the only one. New radio telescope arrays such as the Square Kilometer Array (SKA) under construction will allow for greater sensitivity in searching for weak maser emission in distant targets. Also, new advances in information technology have started a new area of astronomy called astroinformatics. This will involve collecting and correlating large amounts of data from all-sky surveys, improving current data mining techniques. This can be done with optical and infrared data and then quickly referenced with existing radio data (as well as standard monitoring of continuum ra-

dio background) to identify other planetary nebulae with maser characteristics. Once identified, these targets can be observed in detail using the more powerful instruments of SKA and ALMA. The additional data will be helpful in creating models for PN K3-35 and other planetary nebulae.

Bibliography

Carroll, B. W., & Ostlie, D. A. 2007, An Introduction to Modern Astrophysics, 2nd edn. (San Fransisco: Wiley), 470

Cohen, R. 1989, Reports on Progress in Physics, 52, 881

Dopita, M. A., & Sutherland, R. S. 2003, Astrophysics of the Diffuse Universe, 2nd edn. (Springer-Verlag Berlin Heidelberg: Springer), 88

Gomez, Y., Tafoya, D., & Anglada, G. 2009, Astrophysical Journal, 695, 930

Tafoya, D., Gomez, Y., & Anglada, G. 2007, Astronomical Journal, 133, 364

Tafoya, D., Imai, H., & Gomez, Y. 2011, Astronomical Society of Japan, 63, 71

Uscanga, L., Gomez, Y., & Raga, A. 2008, Monthly Notices of the Royal Astronomical Society, 390, 1127

Index